

Harmonic generation by reflecting internal waves

Bruce Rodenborn, D. Kiefer, H. P. Zhang, and Harry L. Swinney

Department of Physics and Center for Nonlinear Dynamics, University of Texas at Austin, Austin, Texas 78712, USA

(Received 20 October 2010; accepted 11 January 2011; published online 11 February 2011)

The generation of internal gravity waves by tidal flow over topography is an important oceanic process that redistributes tidal energy in the ocean. Internal waves reflect from boundaries, creating harmonics and mixing. We use laboratory experiments and two-dimensional numerical simulations of the Navier–Stokes equations to determine the value of the topographic slope that gives the most intense generation of second harmonic waves in the reflection process. The results from our experiments and simulations agree well but differ markedly from theoretical predictions by S. A. Thorpe [“On the reflection of a train of finite amplitude waves from a uniform slope,” *J. Fluid Mech.* **178**, 279 (1987)] and A. Tabaei *et al.* [“Nonlinear effects in reflecting and colliding internal wave beams,” *J. Fluid Mech.* **526**, 217 (2005)], except for nearly inviscid, weakly nonlinear flow. However, even for weakly nonlinear flow (where the Dauxois–Young amplitude parameter value is only 0.01), we find that the ratio of the reflected wave number to the incoming wave number is very different from the prediction of weakly nonlinear theory. Further, we observe that for incident beams with a wide range of angles, frequencies, and intensities, the second harmonic beam produced in reflection has a maximum intensity when its width is the same as the width of the incident beam. This observation yields a prediction for the angle corresponding to the maximum in second harmonic intensity that is in excellent accord with our results from experiments and numerical simulations. © 2011 American Institute of Physics. [doi:10.1063/1.3553294]

I. INTRODUCTION

The reflection of internal waves by topography results in mixing at the boundaries and redistribution of tidal energy in the ocean. The mixing work done by internal waves is hypothesized to be an important source of the potential energy increase needed to return deep, dense water to the surface^{1,2} as part of the meridional overturning circulation,^{3,4} although there is a debate about the importance of vertical mixing in this process.^{5,6}

Wave reflection modifies the internal waves generated by tidal flow over topography. Near the generation region, the wave spectrum includes high harmonic components.⁷ However, high wave modes dissipate rapidly within about 100 km of the generation region.⁸

The processes that both create and dissipate high wave modes are not well understood. Harmonics generated by reflection are a possible source of high wave modes and they may be unstable, causing overturning and mixing. Further, reflection may lead to wave trapping in the boundary layer, another possible source of internal wave mixing. Thus, an understanding of internal wave beam generation and reflection is needed to understand energy transfer in the oceans.

Theoretical work on internal wave reflection has generally been limited to inviscid, weakly nonlinear flow, whereas observations in the oceans, laboratory experiments, and numerical simulations reveal that tidal flow over topography can generate intense, strongly nonlinear wave beams, particularly in regions where the slope of the topography matches the angle of internal wave propagation.^{7,9–15} Dauxois and Young¹⁶ developed a weakly nonlinear theory for

near-critical reflection and concluded that if wave beams are strongly nonlinear, the reflection process will rapidly lead to turbulence and enhanced mixing near the slope. These waves may erode continental slopes to the same angle as internal wave beams at the tidal frequency.^{10,17,18}

Weakly nonlinear analyses for inviscid fluids by Thorpe¹⁹ and by Tabaei *et al.*²⁰ have predicted the value of the topographic slope angle at which the second harmonic intensity is a maximum. Pioneering experiments and simulations^{21,22} studied harmonic generation by reflecting internal waves but did not examine the applicability of the analyses of Thorpe and Tabaei *et al.* to strongly nonlinear reflection processes. The present study examines how the generation of second harmonic waves upon reflection from a sloping boundary depends on boundary angle, wave beam intensity, and fluid viscosity.

This paper is organized as follows. Section II describes the theoretical work of Thorpe and Tabaei *et al.* Section III describes our experimental and computational methods and data analysis. Section IV compares our experimental and numerical results, which agree but differ from the predictions of both of the weakly nonlinear analyses for inviscid fluids. We show that, instead, our results agree with a prediction deduced from an observed geometric relation between the second harmonic and incident wave beams. Section IV also discusses how the results depend on forcing amplitude, viscosity, and frequency. Section V considers the implications of the geometric relation on the reflection of internal waves in theory and in the oceans.

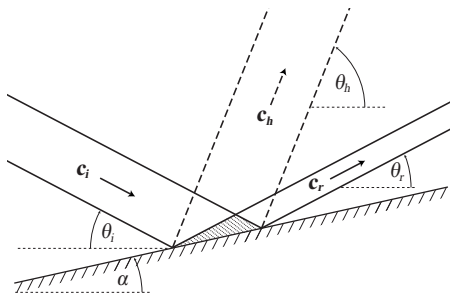


FIG. 1. Schematic showing the reflection of an internal wave beam from a boundary at an angle α relative to the horizontal. The incoming and reflected wave beams are at angles θ_i and θ_r , respectively, which by the dispersion relation (1) are equal because the frequencies ω_i and ω_r are the same. However, the width and wave number of the reflected beam are different than those of the incident beam, as given by Eq. (3). The second harmonic wave beam (shown by the dashed lines) is generated by nonlinear interaction between the incoming and reflected wave beams, which occurs mainly in the overlap (shaded) region. The harmonic propagates at an angle given by $\sin \theta_h = 2\omega/N$. The group velocities \mathbf{c}_i , \mathbf{c}_r and \mathbf{c}_h indicate the direction of energy propagation.

II. THEORY

In a stably stratified fluid, any vertically displaced fluid parcel experiences restoring forces from buoyancy and gravity, causing it to oscillate about its equilibrium height, and this oscillatory motion allows the propagation of internal waves. In the absence of rotation (Coriolis forces), the dispersion relation for plane internal gravity waves is

$$\omega = N \frac{k_x}{\sqrt{k_x^2 + k_z^2}} = N \sin \theta, \quad (1)$$

where ω is the wave frequency, k_x and k_z are, respectively, the horizontal and vertical wave numbers, N is the buoyancy frequency, and θ is the angle of the group velocity relative to the horizontal; θ is also the angle of \vec{k} with respect to the vertical because \vec{k} is perpendicular to the group velocity of the waves (cf. Fig. 1, which uses the notation of Ref. 19). The buoyancy frequency is given by

$$N \equiv \sqrt{-\frac{g}{\rho} \frac{\partial \rho}{\partial z}}, \quad (2)$$

where ρ is the density, g is the gravitational acceleration, and z is the vertical coordinate, aligned antiparallel to the gravity vector.

The dispersion relation (1) is unusual because frequency and wave number are only indirectly related. The profile of an internal wave beam is determined by the wave number distribution of the waves in the packet. The various wave number components in a beam must all have the same frequency because components at different frequencies would travel at different angles and diverge.

In the absence of nonlinear effects, an internal wave beam reflected by a topographic slope must have the same frequency after reflection; hence, it propagates at the same angle with respect to the horizontal as the incident beam, regardless of the angle of the topography from which it reflects (cf. Fig. 1).

The reflected wave beam has a width and wave number profile different from the incident beam because the two beams propagate at the same angle $\theta_r = \theta_i$ (Fig. 1). From ray theory and geometry, the wave numbers are related by

$$\frac{k_i}{k_r} = \frac{\sin(\theta_i - \alpha)}{\sin(\theta_r + \alpha)}. \quad (3)$$

The narrower reflected beam has higher energy flux than the incident beam because the reflected beam is confined within a smaller region. We test the predicted wave number relation (3) in the experiments and simulations described in Sec. IV D and, surprisingly, as we shall show, Eq. (3) fails to describe our results even for our lowest intensity incident beam.

Two approaches have been taken to predict the topographic angle yielding the maximum intensity of the second harmonic. Phillips²³ reasoned that if the fluid is inviscid and nonlinear interactions are weak, the nonlinear process will occur through a resonant triad; that is, a new wave will be generated from the interaction of two internal waves as either the sum or difference of the frequency and of the wave number

$$k_3 = k_1 \pm k_2 \quad \text{and} \quad \omega_3 = \omega_1 \pm \omega_2. \quad (4)$$

Thorpe¹⁹ assumed that harmonic waves result from a resonant triad forming between an incoming *plane wave* and the wave's primary reflection. He used boundary conditions to show that the only angle that satisfies the resonant triad condition is

$$\alpha_{\text{Thorpe}} = \tan^{-1} \left[\left(\frac{\sin \theta_i}{2 \cos^2 \theta_i} \right) \sqrt{-3 + 4 \cos^2 \theta_i} \right]. \quad (5)$$

Although we are concerned with *wave beams*, i.e., a packet of plane waves rather than a single plane wave, we will examine the possible applicability of Thorpe's analysis to our data.

In a different approach, Tabaei *et al.*²⁰ derived a relation for internal wave reflection from a sloping boundary by asymptotically matching solutions in the near and far fields. They considered that for a wave beam, resonant triads can form between any of the components of the incoming and reflected wave beams. For a beam with a Gaussian cross-beam profile in wave number space, the energy of the second harmonic diverges as the angle of the boundary approaches the wave propagation angle.²⁰ Prior to Tabaei *et al.*, the study by Dauxois and Young¹⁶ of near-critical reflection showed that nonlinear and viscous effects heal the singularity that occurs at the critical angle. Thus, the energy will not diverge but will have a large finite value when

$$\alpha_{\text{Tabaei}} = \theta_i. \quad (6)$$

The predictions of Thorpe and Tabaei *et al.* differ significantly, especially for large beam angles. For example, for an incoming wave beam with $\theta_i = 22.7^\circ$, $\alpha_{\text{Thorpe}} = 8.2^\circ$, and $\alpha_{\text{Tabaei}} = 22.7^\circ$. Our experiments and simulations were undertaken to determine which prediction is more accurate.

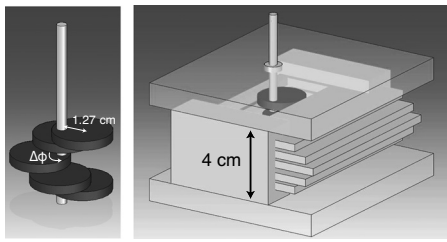


FIG. 2. The wave maker consists of five acrylic plates in a box (right) driven by a camshaft (left) using a computer-controlled stepper motor. The desired beam profile is generated by selecting the angular difference $\Delta\phi$ between successive cams. In this example, $\Delta\phi=45^\circ$, which creates a half-sine wave configuration.

III. METHODS

A. Experiment

Experiments are performed in a 250 l glass tank (90 cm \times 45 cm \times 60 cm high) filled using the double-bucket method²⁴ to create a linearly stratified fluid; this requires about 25 kg of salt (NaCl). The salty water in the bottom of the tank has a viscosity about 30% higher than the fresh water at the top of the tank. However, changes in viscosity are less than 10% within the region studied in the middle of the tank. The density profile, measured with an Anton Paar density meter, is typically linear within 1%. The density change from the top to the bottom is about $\Delta\rho = 140 \text{ kg/m}^3$, which corresponds to a density gradient of $\partial\rho/\partial z = 250 \text{ kg/m}^4$ and a buoyancy frequency of $N = 1.57 \text{ rad/s}$. The internal waves were observed to propagate in straight lines, indicating constant N . The value of N used in comparing experiment and simulation was deduced from the wave propagation angle rather than from the measurements of the density as a function of height.

A collimated internal wave beam is generated using a wave maker similar to the one invented by Gostiaux *et al.*²⁵ The wave maker consists of a stack of five identical acrylic plates (15 cm \times 15 cm \times 0.6 cm), separated by 0.25 cm and housed in a parallelepiped open-sided box (see Fig. 2). A helicoidal rotating camshaft oscillates the plates periodically. The eccentricity of the camshaft determines the oscillation amplitude of the plates. Our velocity field measurements (described below) show that the generated internal wave beam is essentially two-dimensional.

In the tank, the wave maker is pointed in the direction of the excited wave beam. When the frequency, and therefore the wave beam angle, changes, the wave maker tilt angle is adjusted accordingly. The wave beam reflects off an acrylic plate (40 cm \times 20 cm \times 0.6 cm) mounted in the tank. Measurements were made for plate angles ranging from zero (horizontal) to the critical angle ($\alpha = \theta_i$).

Particle image velocimetry is used to measure the velocity field. The fluid is seeded with TiO_2 tracer particles ($\sim 10 \mu\text{m}$ diameter). A 532 nm wavelength laser (0.2–0.5 W) is used to produce a 0.5 cm thick light sheet that illuminates the tracer particles in a vertical plane.

The tracer particle motion in a 25 cm \times 25 cm region is imaged with a 10 bit digital camera (resolution: 1004 \times 1004 pixels). The instantaneous velocity field is ex-

tracted from consecutive image pairs using the CIV algorithm of Fincham and Delerce.²⁶ The algorithm is run with a MATLAB interface and the velocity field is stored in a Network Common Data Form file. Data analysis is done in MATLAB either using the UVMAT interface or our own MATLAB codes.

B. Numerical simulations

Our numerical simulations use a slightly modified version of a code developed by Barranco and Marcus.²⁷ This pseudospectral, fully parallelized code describes a two-dimensional, stratified fluid in the Boussinesq approximation, which is valid for flow in our tank because the variation in density is small. The code solves for the three components of the velocity and the density with a fractional step method. The equations solved are

$$\partial \vec{u} / \partial t = -(\vec{u} \cdot \nabla) \vec{u} - \nabla P / \rho_0 - g \hat{n} (\rho / \rho_0) + \nu \nabla^2 \vec{u}, \quad (7)$$

$$\nabla \cdot \vec{u} = 0, \quad (8)$$

$$\partial \rho / \partial t = -(\vec{u} \cdot \nabla) \rho + (\rho_0 N^2 / g) u_z, \quad (9)$$

where \vec{u} is the velocity, u_z is the vertical component of the velocity, P is the nonhydrostatic component of the pressure, ρ is the nonhorizontally averaged density perturbation, N is the buoyancy frequency as defined in Eq. (2), \hat{n} is a unit vector that points vertically upward (antiparallel to gravity), and ν is the kinematic viscosity.

To generate internal gravity waves, a momentum forcing term similar to that used by Slinn and Riley²⁸ and Javam *et al.*²⁹ is added to the right side of Eq. (7)

$$\vec{F} = [\nabla \times (\nabla \times \Phi \hat{z})] \cos(\omega t + \phi), \quad (10)$$

where ω and ϕ are, respectively, the forcing frequency and phase. The amplitude Φ_{max} , position (x_0, z_0) , and beam width σ (standard deviation of the Gaussian profile) of the forcing are given through the term

$$\Phi(x, z) = \Phi_{\text{max}} \exp \left[\frac{-(x - x_0)^2 - (z - z_0)^2}{2\sigma^2} \right]. \quad (11)$$

We use the code to solve the full Eqs. (7)–(9) directly in two dimensions for Reynolds numbers up to several thousand, which is beyond the highest Reynolds number (about 1000) reached in our laboratory experiments. The computations yield the x and z components of the velocity and the y component of vorticity at each grid point, 128 times per wave period. The instantaneous vorticity field of a numerically simulated internal wave field is shown in Fig. 3. The forcing is strongest along the wave beam propagation direction (in the second and fourth quadrants with respect to the wave maker), though weaker beams can be seen in the other two quadrants.

The Reynolds number dependence of the results was examined by solving the equations for different values of the viscosity ν and for different beam widths σ . For some tests, we use an inviscid version of the code with the no-slip boundary conditions at boundaries A and C replaced with free-slip boundary conditions.

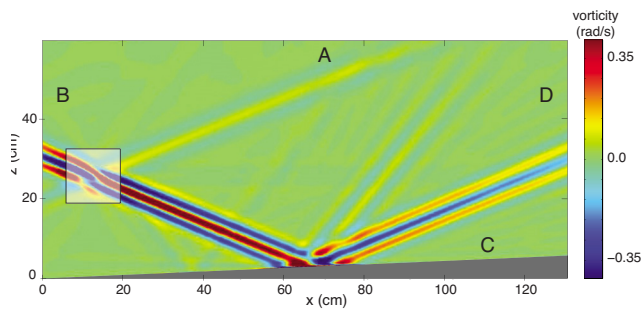


FIG. 3. (Color online) Vorticity field computed for $\theta_i=22.7^\circ$, $N=1.63$ rad/s, $\nu=0.01$ cm²/s, and plate angle $\alpha=2.5^\circ$. The computational domain has been rotated so that the gravity vector points downward; the image has been cropped to fit. The shaded box shows the location of the forcing term. A sponge layer has been added to the no-slip boundary at the top of the domain (boundary A) to absorb the upward propagating wave created by the wave maker. The simulation is periodic at boundaries B and D and there is a no-slip boundary condition at boundary C.

In both simulation and experiment, the beam intensity for a given forcing depended slightly on the domain size and the bottom boundary angle relative to the horizontal. To ensure that all incident wave beams used in a beam angle study were the same, the finite domain effects were controlled by adjusting the amplitude and/or wavelength. The peak vorticity of the beam incident on the plate was kept at ≈ 0.4 rad/s just before hitting the boundary; this corresponds to a velocity amplitude $|\vec{u}_{\max}| \approx 0.25$ cm/s. As Fig. 4 illustrates, the beam profiles of the instantaneous vorticity and the velocity amplitude from experiment and simulation are nearly the same.

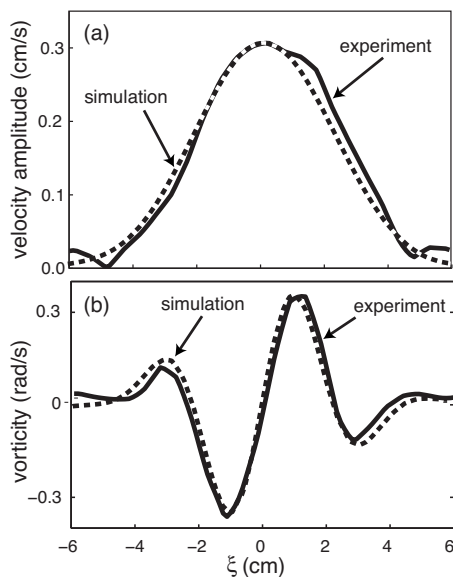


FIG. 4. (a) The time-independent velocity amplitude cross sections for wave beams under the same conditions as in Fig. 6. The cross section from the numerical simulation (dashed line) is accurately Gaussian, whereas there is a small departure from a Gaussian for the laboratory beam (solid line). (b) Vorticity cross section snapshots at the same location.

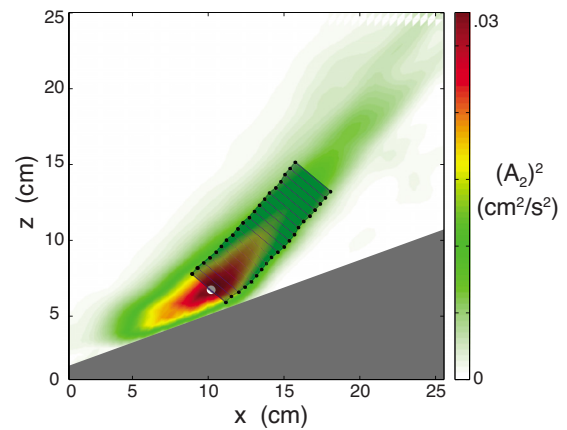


FIG. 5. (Color online) Contour plot of the measured second harmonic intensity $(A_2)^2$. The kinetic energy of the beam was integrated over the area where it was above one-half the maximum. Integration starts at the point of maximum kinetic energy within the beam (white circle).

C. Data analysis

In the experiments and simulations, we found that the reflection process evolved to a steady state in about eight oscillation periods. The analysis was done after waiting 15 wave periods, well after steady state had been achieved but before the reflection region became affected by multiple reflections from side and top boundaries.

To find the steady state velocity amplitude in the experiments and simulations, each component (u_x and u_z) of the velocity field is first processed in MATLAB using a four-parameter curve fit to

$$u = A_1 \sin(\omega + \phi_1) + A_2 \sin(2\omega + \phi_2), \quad (12)$$

where u refers to one of the two velocity components, A_1 is the amplitude at the fundamental frequency ω , A_2 is the amplitude at the harmonic frequency 2ω , and ϕ_1 and ϕ_2 are the corresponding phases.

As a measure of the intensity of the second harmonic wave beam generated by reflection for different plate angles α , we integrate $(A_2)^2$ in the approximately rectangular region shown in Fig. 5, where the beam amplitude is computed from $(A = \sqrt{A_x^2 + A_z^2})$.

The resultant kinetic energy depends on the starting point of the integration, so for consistency, we used the point of highest kinetic energy as the starting point (cf. Fig. 5). The location of maximum kinetic energy was found using $(A_2)^2$ as the weights in an average over the highest energy region of the beam (dark red in Fig. 5)

$$\vec{r}_{\max KE} = \frac{\sum_i A_i^2 \vec{r}_i}{\sum_i A_i^2}, \quad (13)$$

where A_i is the amplitude and \vec{r}_i is the position coordinate for the i th grid point within the region.

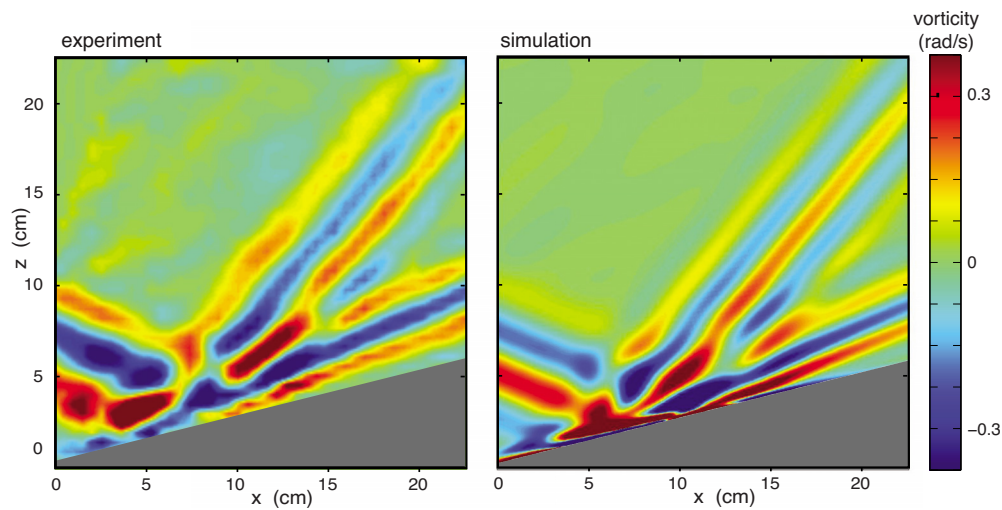


FIG. 6. (Color online) Instantaneous experimental and computed vorticity fields for forcing frequency, $\omega=0.628$ rad/s, $N=1.63$ rad/s, $\theta_i=22.7^\circ$, plate angle $\alpha=14.1^\circ$, and beam amplitude $A\sim 0.25$ cm/s. In the experiment, the spatial resolution was 0.5 cm.

IV. RESULTS

A. Intensity of second harmonic from experiment and simulation

Our experimental and computational results for the vorticity fields of reflecting internal wave beams agree well, as the snapshots in Fig. 6 illustrate. The intensity of the second harmonic generated by the beam reflection as the plate angle α varied was found in all cases to exhibit a well-defined maximum (Fig. 7), which contrasts with an earlier observation²² that did not detect any boundary angle dependence of the second harmonic intensity. In our experiments and simulations, the angles determined for the maximum second harmonic intensity agreed within 1° , although the experiments and simulations yielded a somewhat different functional dependence of the intensity on plate angle (Fig. 7). This difference arose in part because of the experimental difficulty in maintaining the same incident beam waveform for varying distances between the wave maker and the re-

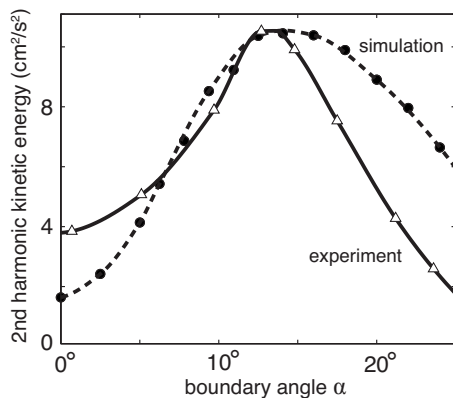


FIG. 7. Intensity of the second harmonic generated in the reflection of an internal wave beam (at $\theta=22.7^\circ$) from a plate tilted at angle α . The curves are cubic spline fits to the data. The boundary angles α where the maxima occur are $\alpha_{\max}=13.2^\circ$ (experiment) and 14.1° (simulation), far from either the 22.7° predicted by Tabaei *et al.* (Ref. 20) or the 8.25° predicted by Thorpe (Ref. 19).

flecting plate for different plate angles; the waveform also depended on the oscillation amplitude of the wave maker and on finite domain effects, which changed with plate angle. Further, the simulations were two-dimensional whereas the experiments were only approximately so.

In all weakly nonlinear theories, the amplitude of the second harmonic varies as the square of the amplitude of the incident beam. Figure 8(a) shows this expected quadratic dependence for low amplitude incident beams, but for high amplitude incident beams, the amplitude of the second harmonic saturates. To characterize the degree of nonlinearity, we use the dimensionless amplitude parameter introduced by Dauxois and Young¹⁶ in a two-dimensional theoretical study of near-critical reflection

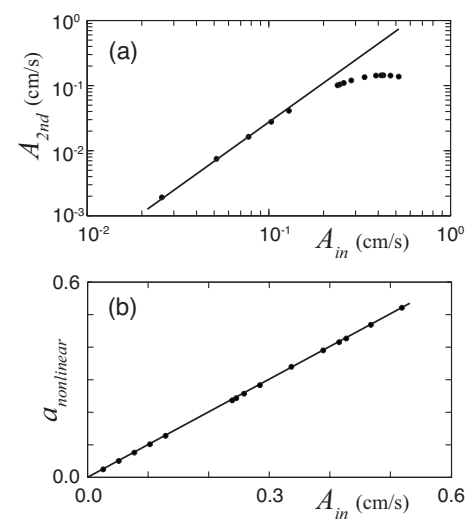


FIG. 8. (a) The second harmonic amplitude depends quadratically (black line) on the incident wave beam amplitude, up to high amplitudes where the second harmonic determined in the simulations (solid dots) saturates (for a beam incident at $\theta=22.7^\circ$ on a boundary at angle $\alpha=12.5^\circ$). (b) Under the same conditions, the dimensionless amplitude parameter $a_{\text{nonlinear}}$ [Eq. (14)] in the simulations varied from 0.01 (very weakly nonlinear) to 0.52 (nonlinear) and in the experiments was 0.25 (corresponding to $A_{\text{in}}=0.25$ cm/s).

$$a_{\text{nonlinear}} \equiv \frac{k_{\text{in}}^2 \sin[2(\theta + \alpha)]}{2N \sin \theta} \psi_{\text{max}}, \quad (14)$$

where k_{in} is the magnitude of the wave vector of the incident beam, ψ_{max} is the maximum amplitude of the stream function, and α and θ are defined in Fig. 1. Weakly nonlinear theory should apply when $a_{\text{nonlinear}} \ll 1$, but in our experiments $a_{\text{nonlinear}} \approx 0.25$ and simulations were conducted for $0.01 < a_{\text{nonlinear}} < 0.5$ [see Fig. 8(b)]. We shall show in Sec. IV D that our simulations reveal a significant departure from weakly nonlinear theory even for $a_{\text{nonlinear}} = 0.01$.

B. An observation-based prediction in accord with experiment and simulation

We find that for every internal wave beam that we could produce in experiment and for all but the lowest intensity beams in the simulations, the second harmonic generated in reflection has a maximum intensity when the width of this beam is the same as that of the incident beam. This result, found for a wide range of incident beam intensities, widths, and angles, leads to the conclusion from ray theory that the plate angle corresponding to the maximum intensity of the second harmonic beam is given by

$$\alpha_{\text{geom}} = \frac{\tan^{-1}(\sin \theta_i)}{\sqrt{1 - 4 \sin^2 \theta_i + \cos \theta_i}}, \quad (15)$$

which is in remarkable accord with our laboratory and computational results [Fig. 9(a)]. For higher plate angles, those near critical, we observed very weak second harmonic waves and strong mean flows from the reflection region. However, we did not observe density inversions or turbulent events.

C. Recovery of the Tabaei *et al.* prediction for low amplitude beams

The analyses of Thorpe and Tabaei *et al.* (cf. Sec. II) assumed weak nonlinearity and no viscosity. To examine this limit we simulated wave beams of very low intensity ($A_{\text{in}} \sim 0.01$ cm/s and $a_{\text{nonlinear}} \sim 0.01$), below the level for which we were able to make accurate measurements in our experiments. The results then agreed with the Tabaei *et al.* prediction for beam angles down to about $\theta \geq 20^\circ$ and reducing the fluid viscosity led to agreement with Tabaei *et al.* to yet lower beam angles [Fig. 9(b)]. However, as the wave amplitude was increased, α_{max} decreased rapidly, departing from the prediction of Tabaei *et al.* For lower frequency waves, we found that the amplitude of the incident beam had to be even lower for α_{max} to approach the Tabaei *et al.* prediction. Tabaei *et al.*²⁰ comment that nonlinear effects are generally increased by longer time scales of interaction; this is supported by the dependence on wave period we found.

D. Wave number and amplitude of the reflected fundamental beam

The results from our experiments and simulations show that the weakly nonlinear analyses of Thorpe¹⁹ and Tabaei *et al.*²⁰ have limited applicability. To understand this result, we measured the wave number of the incident beam and the

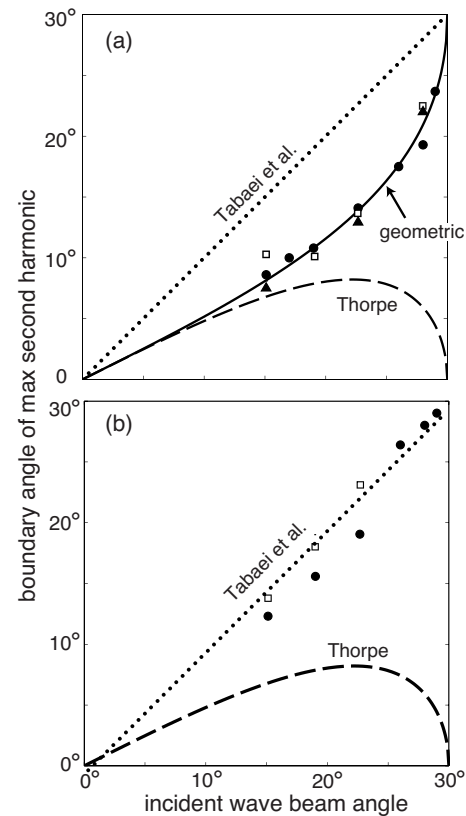


FIG. 9. The boundary angle corresponding to the maximum intensity of the second harmonic of an internal wave beam reflected from a surface for incident beam velocity amplitudes: (a) $A=0.25$ cm/s ($a_{\text{nonlinear}}=0.25$) and (b) $A=0.01$ cm/s ($a_{\text{nonlinear}}=0.01$). Our laboratory observations (triangles), numerical simulations (circles) with water viscosity ($\nu=0.01$ cm²/s), and numerical simulations with viscosity reduced by an order of magnitude (open squares) in (a) all agree well with the solid curve [Eq. (15)], which was obtained from ray theory, given the observation that the maximum intensity of second harmonic occurs when that beam's width is the same as that of the incident beam. Clearly, these results do not agree with the theory of Tabaei *et al.* (Ref. 20) or Thorpe (Ref. 19). However, for beams of very low velocity amplitude ($A=0.01$ cm and $a_{\text{nonlinear}}=0.01$, well below the experimentally measurable level) in (b) agree with the prediction of Tabaei *et al.* for incident beam angles greater than $\sim 25^\circ$. When the viscosity is reduced from that of water by an order of magnitude, the agreement of the simulation with the prediction of Tabaei *et al.* extends to about 15° (open squares).

reflected fundamental beam to test the assumption in the Thorpe and Tabaei *et al.* analyses that the incident and reflected beams have wave numbers in the ratio given by Eq. (3). We determined the wave numbers of the beams by fitting the cross-sectional profiles of the vorticity to

$$q = q_{\text{max}} \{ \exp[-(\eta - \eta_0)^2 / 2\sigma^2] \} \sin(k\eta + \phi), \quad (16)$$

where q_{max} is the amplitude of oscillation, η is a coordinate perpendicular to the wave beam propagation direction, η_0 is the center of the wave beam, σ is the standard deviation of the wave packet envelope, k is the dominant wave number in the beam, and ϕ is the phase at a given instant in time.

Equation (3) predicts that the wave number ratio k_i/k_r should approach zero as the critical angle is approached, whereas our simulations yield a quite different result: the ratio k_i/k_r remains far above zero as the boundary angle increases toward the incident beam angle, as shown in

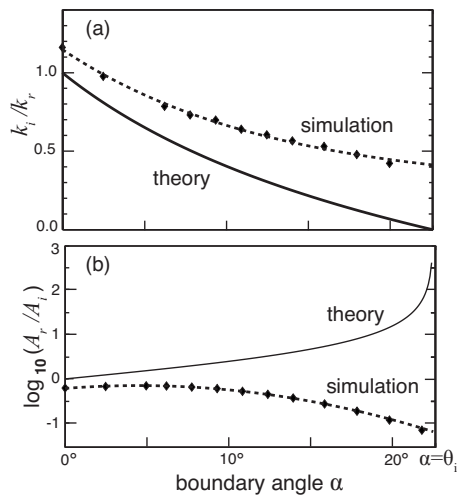


FIG. 10. (a) The ratio of the dominant wave number in the incoming beam to the dominant wave number of the reflected beam (at the fundamental frequency) given by theory [Eq. (3), solid curve] and numerical simulation (dashed curve). (b) The prediction of the theory of Tabaei *et al.* for the ratio of the reflected fundamental wave beam's peak amplitude to the incoming wave beam's peak amplitude, $A_r/A_i = \sin(\theta_r + \alpha)/\sin(\theta_i - \alpha)$, compared with the results from our numerical simulation. Theory predicts that the amplitude of the reflected wave should diverge at the critical angle, whereas the simulations yield quite different behavior with a broad peak in the reflected wave amplitude at about $\alpha = 4.5^\circ$ and a monotonic decrease in amplitude for larger angles. [In both (a) and (b), $\theta_i = 22.7^\circ$, $A_{in} = 0.25$ cm, and $a_{nonlinear} = 0.25$.]

Fig. 10(a). The laboratory measurements of the wave number ratio are consistent with the simulations for the same incident beam amplitude. Simulations were then made with the amplitude parameter $a_{nonlinear}$ reduced from 0.25, as in Fig. 8, to a value of only 0.01 and the viscosity reduced to a value ten times smaller than that of water, but the wave number ratio limit decreased only a small amount, from 0.40 to 0.35.

Another prediction of the theory of Tabaei *et al.* (but not that of Thorpe¹⁹) is that the amplitude of the reflected wave beam should be given by $A_r/A_i = \sin(\theta_r + \alpha)/\sin(\theta_i - \alpha)$, thus diverging at the critical angle. Instead, our simulations yield very different behavior, as Fig. 10(b) illustrates. Thus we conclude that even when the theory of Tabaei *et al.* predicts the angle found for the maximum second harmonic intensity (at low intensities, cf. Sec. IV B), the predictions about the wave number and the amplitude of reflected fundamental wave beam are not valid.

E. Wave number of the second harmonic

The analyses of Thorpe¹⁹ and Tabaei *et al.*²⁰ predict that a harmonic generated in reflection should have a wave vector component parallel to the boundary that is simply related to the incident beam's wave vector component parallel to the boundary $k_{||} = nk_{i||}$, where n is the order of the harmonic. Gostiaux *et al.*²² confirmed this prediction experimentally and our experiments and simulations are also in accord with the predicted relation. It seems plausible that this result, coupled with the α_{geom} condition (equal beam widths at peak harmonic generation), would lead to a triad relationship between the wave vectors of the incident, reflected fundamental, and reflected harmonic, as expected from the resonant

triad theory of Thorpe;¹⁹ however, the results for the wave vectors in our experiments and simulations do not support the triad theory.

F. Reflection compared to interaction of unbounded beams

Although Eq. (3) does not correctly predict the characteristics of the reflected wave beams, harmonic generation might still result from the nonlinear interaction of the incoming and reflected wave beams. The process is analogous to the incoming wave beam interacting with a virtual wave beam emanating from the bottom boundary with the same characteristics as the reflected wave. Such beam-beam interactions will create harmonic waves except for certain beam orientations as shown by Jiang and Marcus.³⁰ We simulated such colliding wave beams (in the absence of a reflecting boundary) with the amplitude and wave number profile of the interacting beams matched to those of the incoming and reflected wave beams from the simulations.

Our numerical simulations reveal that the intensity of the second harmonic is proportional to the sum of the integrated intensities (see Sec. III C) of the incident beam and the reflected fundamental wave beam. Hence, harmonic generation is strongest when the virtual reflected wave beam is the strongest since the incoming wave beam is held fixed. As shown in Fig. 10, the reflected wave beam has the highest amplitude (and highest integrated kinetic energy because it is also relatively wide) at a small angle of α , not at the critical angle. Thus, our data cannot be explained as a nonlinear self-interaction between the incoming and reflected wave beams, as suggested by Phillips.^{23,31}

V. DISCUSSION

Our laboratory experiments and numerical simulations for an internal wave reflecting from a sloping boundary are in good agreement [Fig. 9] and they reveal a distinct peak in the second harmonic intensity as the boundary angle varies. Our results differ from the predictions by Tabaei *et al.*,²⁰ except for very weak forcings, weaker than those measurable in experiments, in which case we recover the results of Tabaei *et al.* for wave beam angles greater than $\sim 25^\circ$, i.e., the boundary angle of maximum harmonic generation approaches the critical angle. This agreement extended to somewhat lower wave beam angles when the fluid viscosity was decreased by an order of magnitude. However, we found that even for low intensity incident beams ($a_{nonlinear} \sim 0.01$), the result from our simulation differs from the weakly nonlinear theory prediction for the wave number ratios k_i/k_r [cf. Fig. 10(a)].

We did not find agreement with the resonant triad prediction of Thorpe¹⁹ for any conditions, likely because as pointed out in Sec. II, Thorpe derived his result for a plane wave reflecting from a boundary, not for a packet of plane waves (finite extent wave beam), where there are interactions that depend on the wave number profile of the wave beam.

Neither the theory of Tabaei *et al.* nor Thorpe correctly predicts the boundary angle that maximizes the generation of second harmonic waves in the laboratory experiments or nu-

merical simulations. However, we obtained a prediction [Eq. (15)] for the angle of maximum second harmonic intensity in good agreement with our results from experiment and simulations; our prediction was based on the observation that when the second harmonic has maximum intensity, the widths of the incoming and second harmonic beams are equal (cf. Sec. IV C). Importantly, Eq. (15) holds with the viscosity reduced by an order of magnitude, and this result is correlated with long wave period. Thus, it may be relevant in the ocean since wave beams near the generation region are intense and have long wave periods that are of the order of the tidal forcing period.^{12,32} Further, wave beams generated by tidal flow over topography in a stratified fluid have a profile similar to those generated in our experiments and simulations.¹⁵

Our results indicate that critically reflecting internal waves (where $\theta = \alpha$), rather than being a source of intense second harmonic waves, dissipate energy in the boundary region. Although our experiments and simulations are for nonlinear waves (i.e., they are not described by weakly nonlinear theory), we did not observe strongly nonlinear phenomena such as density inversions, turbulent events, or other direct evidence of mixing. However, we did observe strong mean flows propagating from the reflection region. The observed mean flows are similar to the strong boundary currents found by Eriksen³³ and observed for tidal flow on topography where the slope is near the critical angle.^{10,14} Recent observations by van Haren and Gostiaux³⁴ provide direct evidence of breaking tidal-frequency internal waves along a seamount. They show that the process involves the coupling of low-frequency tidal waves with high-frequency internal waves near the buoyancy frequency. This result suggests that internal wave reflection is an important part of the ocean mixing process.

ACKNOWLEDGMENTS

We gratefully acknowledge the theoretical and computational support from P. J. Marcus and C. H. Jiang of the University of California Berkeley. This research was supported by the National Science Foundation Grant No. CBET-0755114.

¹J. R. Ledwell, E. T. Montgomery, K. L. Polzin, L. C. St. Laurent, R. W. Schmitt, and J. M. Toole, "Evidence for enhanced mixing over rough topography in the abyssal ocean," *Nature (London)* **403**, 179 (2000).

²R. Ferrari and C. Wunsch, "Ocean circulation kinetic energy: Reservoirs, sources, and sinks," *Annu. Rev. Fluid Mech.* **41**, 253 (2009).

³C. C. Eriksen, "Implications of ocean bottom reflection for internal wave spectra and mixing," *J. Phys. Oceanogr.* **15**, 1145 (1985).

⁴C. Wunsch and R. Ferrari, "Vertical mixing, energy and the general circulation of the oceans," *Annu. Rev. Fluid Mech.* **36**, 281 (2004).

⁵J. R. Toggweiler and B. Samuels, "On the ocean's large-scale circulation near the limit of no vertical mixing," *J. Phys. Oceanogr.* **28**, 1832 (1998).

⁶C. L. Wolfe, J. L. McClean, and M. E. Maltrud, "Vertical heat transport in eddy ocean models," *Geophys. Res. Lett.* **35**, L23605 (2008).

⁷S. Legg, "Internal tides generated on a corrugated continental slope. Part I: Cross-slope barotropic forcing," *J. Phys. Oceanogr.* **34**, 156 (2004).

⁸R. D. Ray and G. T. Mitchum, "Surface manifestation of internal tides generated near Hawaii," *Geophys. Res. Lett.* **23**, 2101 (1996).

⁹P. G. Baines, "On internal tide generation models," *Deep-Sea Res., Part A* **29**, 307 (1982).

¹⁰D. A. Cacchione, L. F. Pratson, and A. S. Ogston, "The shaping of continental slopes by internal tides," *Science* **296**, 724 (2002).

¹¹K. G. Lamb, "Nonlinear interaction among internal wave beams generated by tidal flow over supercritical topography," *Geophys. Res. Lett.* **31**, L09313 (2004).

¹²C. Garrett and E. Kunze, "Internal tide generation in the deep ocean," *Annu. Rev. Fluid Mech.* **39**, 57 (2007).

¹³S. A. Thorpe, *The Turbulent Ocean* (Cambridge University Press, Cambridge, 2005).

¹⁴H. P. Zhang, B. King, and H. L. Swinney, "Experimental study of internal gravity waves generated by supercritical topography," *Phys. Fluids* **19**, 096602 (2007).

¹⁵B. King, H. P. Zhang, and H. L. Swinney, "Tidal flow over three-dimensional topography generates out-of-forcing-plane harmonics," *Geophys. Res. Lett.* **37**, L14606 (2010).

¹⁶T. Dauxois and W. Young, "Near-critical reflection of internal waves," *J. Fluid Mech.* **390**, 271 (1999).

¹⁷P. Puig, A. Palanques, J. Guillen, and M. El Khatab, "Role of internal waves in the generation of nepheloid layers on the northwestern alboran slope: Implications for continental margin shaping," *J. Geophys. Res., [Oceans]* **109**, C09011, doi:10.1029/2004JC002394 (2004).

¹⁸H. P. Zhang, B. King, and H. L. Swinney, "Resonant generation of internal waves on a model continental slope," *Phys. Rev. Lett.* **100**, 244504 (2008).

¹⁹S. A. Thorpe, "On the reflection of a train of finite amplitude waves from a uniform slope," *J. Fluid Mech.* **178**, 279 (1987).

²⁰A. Tabaei, T. R. Akylas, and K. G. Lamb, "Nonlinear effects in reflecting and colliding internal wave beams," *J. Fluid Mech.* **526**, 217 (2005).

²¹T. Peacock and A. Tabaei, "Visualization of nonlinear effects in reflecting internal wave beams," *Phys. Fluids* **17**, 061702 (2005).

²²L. Gostiaux, T. Dauxois, H. Didelle, J. Sommeria, and S. Viboud, "Quantitative laboratory observations of internal wave reflection on ascending slopes," *Phys. Fluids* **18**, 056602 (2006).

²³O. M. Phillips, *The Dynamics of the Upper Ocean* (Cambridge University Press, Cambridge, 1977).

²⁴G. Oster, "Density gradients," *Sci. Am.* **213**, 70 (1965).

²⁵L. Gostiaux, H. Didelle, S. Mercier, and T. Dauxois, "A novel internal waves generator," *Exp. Fluids* **42**, 123 (2007).

²⁶A. Fincham and G. Delerce, "Advanced optimization of correlation imaging velocimetry algorithms," *Exp. Fluids* **29**, S13 (2000).

²⁷J. A. Barranco and P. S. Marcus, "A 3d spectral anelastic hydrodynamic code for shearing, stratified flows," *J. Comput. Phys.* **219**, 21 (2006).

²⁸D. N. Slinn and J. J. Riley, "A model for the simulation of turbulent boundary layers in an incompressible stratified flow," *J. Comput. Phys.* **144**, 550 (1998).

²⁹A. Javam, J. Imberger, and S. W. Armfield, "Numerical study of internal wave reflection from sloping boundaries," *J. Fluid Mech.* **396**, 183 (1999).

³⁰C. H. Jiang and P. S. Marcus, "Selection rules for the nonlinear interaction of internal gravity waves," *Phys. Rev. Lett.* **102**, 124502 (2009).

³¹O. M. Phillips, "Energy transfer in rotating fluids by reflection of inertial waves," *Phys. Fluids* **6**, 513 (1963).

³²P. E. Holloway and M. A. Merrifield, "Internal tide generation by seamounts, ridges, and islands," *J. Geophys. Res.* **104**, 25,937, doi:10.1029/1998JA900059 (1999).

³³C. C. Eriksen, "Observations of internal wave reflection off sloping bottoms," *J. Geophys. Res., C: Oceans Atmos.* **87**, 525, doi:10.1029/JC087iC01p00525 (1982).

³⁴H. van Haren and L. Gostiaux, "A deep-ocean Kelvin-Helmholtz billow train," *Geophys. Res. Lett.* **37**, L03605 (2010).